

# Direct Simulation of Surface Roughness Effects with RANS and DES Approaches on Viscous Adaptive Cartesian Grids

Z.J. Wang\* and X.K. Chi†

*Department of Mechanical Engineering, Michigan State University, East Lansing, MI 48824*

Tom Shih‡

*Department of Aerospace Engineering, Iowa State University, Ames, IA 50011-2271*

and

Jeffrey Bons§

*Department of Mechanical Engineering, Brigham Young University, Provo, Utah 84602-4201*

The main objective of this research is to directly compute the skin friction ( $c_f$ ) and heat transfer ( $St$ ) coefficients on real rough surfaces using a state-of-the-art unstructured adaptive grid-based finite volume method. Recent experiments with real roughness panels by Bons are computationally simulated in this study. Computational results are compared with experimental data to assess the simulation accuracy. A RANS (Reynolds-Averaged Navier-Stokes) approach based on the Spalart-Allmaras turbulence model and a DES (Detached Eddy Simulation) approach are employed for the computations, and grid refinement studies are conducted to assess the effects of grid resolution. In two cases with rough surfaces, the RANS approach is capable of accurately predicting  $c_f$  (within 3.5%) while under-predicting  $St$  by 8-15%. The DES approach was able to predict  $c_f$  and  $St$  for smooth flat panels but failed in the cases with real roughness. The cause will be further investigated.

## Nomenclature

$c_f$	=	skin friction coefficient, $\tau_w / (0.5\rho U_\infty^2)$
$h$	=	convective heat transfer coefficient
$k^+$	=	$k_s u_\tau / \nu \equiv Re_k$
$k$	=	average roughness height ( $\approx Rz$ )
$k_s$	=	equivalent sandgrain roughness
$Rq$	=	rms roughness
$Re$	=	Reynolds number
$Re_x$	=	Reynolds number $U_\infty x / \nu$
$Pr$	=	Prandtl number ( $\nu/\alpha$ ) (= 0.71)
$Pr_t$	=	turbulent Prandtl number (= 0.9)
$St$	=	Stanton Number, $h / (\rho c_p U_\infty)$
$u_\tau$	=	friction or shear velocity $\sqrt{\tau_w / \rho}$
$x$	=	streamwise distance from tunnel floor leading edge
$\delta$	=	boundary layer thickness
$\Lambda_s$	=	roughness shape/density parameter

---

\* Associate Professor of Mechanical Engineering, 2555 Engineering Building, Associate Fellow of AIAA

† Graduate Student, 2555 Engineering Building, Student Member of AIAA

‡ Professor and Chair, Department of Aerospace Engineering, Associate Fellow of AIAA

§ Associate Professor of Mechanical Engineering, Member of AIAA

## I. Introduction

Components of land-based gas turbines operate in a particularly harsh environment. All surfaces such as blades, vanes, end-walls, and hubs that come in contact with the combustor's hot gases invariably become rough with service. The degree and the nature of the roughness due to mechanisms such as erosion, fuel deposition, pitting, and spallation of thermal-barrier coatings depend on the environment from which the air is ingested, the operating conditions, the effectiveness of cooling management such as film cooling in maintaining material temperatures within acceptable limits, and the service time. This material degradation in the form of surface roughness is known to increase surface skin friction and heat transfer in a significant way. For a given cooling management, increase in surface heat transfer increases material temperature, which hastens further material degradation. In order to estimate the service life of turbine blades, it is necessary to estimate the skin friction and heat transfer augmentation generated by various types of surface roughness.

The importance of surface roughness on surface skin friction and heat transfer has led many investigators to study this problem. Methods of study fall roughly into two major categories: experimental and computational modeling approaches. Because surface roughness depends on so many factors, it is nearly impossible to design "artificial roughness" which approximates true surface roughness observed on turbine blades with high fidelity. As a result, many researchers have used relatively simple surface models such as distributed cylinders<sup>1,2</sup>, spherical segments<sup>3,4</sup>, cones<sup>5,6</sup>, and pedestals<sup>7</sup>, all of which achieved a varying degree of success. Because of the high cost associated with conducting experiments, computational modeling of the surface roughness effects on skin friction and heat transfer has become a preferred approach. In a computational modeling approach, surface roughness of a given turbine blade is described with a few parameters, such as the average roughness height  $k$ , the equivalent sandgrain roughness  $k_s$ , or the rms roughness  $R_q$ . Correlation formulas are then derived based on past experience and experimental data. However, the applicability of these correlations is invariably limited. For example, large errors are produced when correlation formulas for  $c_f$  and  $St$  are applied to real roughness panels investigated by Bons<sup>8,9</sup>.

In this study, we attempt to directly compute the skin friction and heat transfer on rough surfaces by solving the Navier-Stokes equations. In addition, the "real" rough surface geometry is preserved by the computational grid in order to minimize the uncertainty associated with artificial surface roughness. This undertaking is made possible by a recent experiment performed by Bons<sup>9</sup> using properly scaled, measured surface roughness of turbine components in long time service. Detailed measurements of  $c_f$  and  $St$  were made, which can serve as validation data for computational simulations. In the experiment, several rough surface panels were placed in a wind tunnel, and  $c_f$  and  $St$  were measured with specially designed experimental instruments. To compute this flow directly is a challenge because of the disparate length scales in the physical problem. First, there is the model length scale,  $L$ , in the present case the length of the wind tunnel. Second, there is a feature length associated with a typical roughness element,  $l$ , which is 3 or 4 orders less than  $L$ . Lastly, there is the thickness of the viscous sub-layer,  $\delta_v$ , which is 5-6 orders less than  $L$ . It is critical that all three length scales are captured in the computational grid to achieve any computational success. In computational fluid dynamics (CFD), the disparity between  $L$  and  $\delta_v$  can be efficiently captured by one-dimensional grid clustering near solid walls in the wall normal direction. For the computational grid to capture rough elements, the grid size along the tangential direction of the rough wall must be comparable to  $l$ . If one uses a non-adaptive structured grid, and employs 50 points in the wall normal direction, the grid size is expected to be roughly  $1,000 \times 1,000 \times 50$  ( $5 \times 10^7$  points), which will overwhelm most computer clusters. A far more efficient computational grid for this type of geometry is an unstructured adaptive grid. It appears a recent adaptive grid approach named viscous adaptive Cartesian approach<sup>10</sup> is the most suitable to tackle the challenge. A finite volume Navier-Stokes solver<sup>11</sup> capable of handling viscous adaptive Cartesian grids will be employed to carry out the computational simulations with both RANS<sup>12,13</sup> (Reynolds-averaged Navier-Stokes) and DES (Detached Eddy Simulation) approaches to model flow turbulence. The DES<sup>14,15,16</sup> approach is a hybrid RANS/LES (large eddy simulation) approach designed to capture both the boundary layer and large separation regions. The reason for using both RANS and DES approaches is to compare the computational results of both with experimental data to see which achieves a better agreement. If validated successfully with experimental data, the present approach can be used to generate extensive data to assist and improve computational model development.

The paper is organized as follows: In the next section, Section II, the experimental setup is reviewed to set the stage for computational simulations. In Section III, the viscous adaptive Cartesian grid generation approach is briefly described. Section IV presents the basic features of the finite-volume Navier-Stokes solver with a RANS Spalart-Allmaras (S-A) model and the DES approach. In Section V, a validation case is first presented and direct simulations including the surface roughness are performed, and the results are compared to experimental data. Finally conclusions from the present are summarized in Section VI.

## II. Experimental Setup

In Bons' wind tunnel experiments<sup>9</sup>, six different rough surfaces were tested. These surfaces were selected by the manufacturers as to be representative of general surface conditions of land-based gas turbines. They include one pitted surface, two coated/spalled surfaces, one fuel deposit surface, and two erosion/deposit surfaces. In the present computational study, two surfaces, Surface #4 and #6, out of the six are selected. Surface #4 is an example surface with fuel deposits that are elliptical in shape and aligned with the stream-wise direction, and is shown in Figure 1. Geometry of Surface #4. Surface #6 is representative of combined erosion and deposits surface with smaller, more jagged roughness elements than surface #4. Nikuradse<sup>17</sup> classified roughness into three regimes based on  $k^+$ : aerodynamically smooth ( $k^+ < 5$ ), transitionally rough ( $5 < k^+ < 70$ ), and completely rough ( $k^+ > 70$ ). The surface data were properly scaled to make sure the scaled model and the actual parts have the same roughness regime as defined by  $k^+$ .

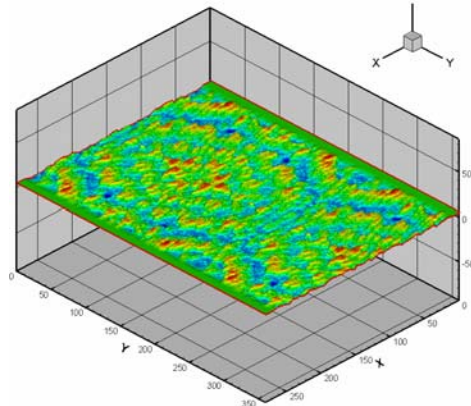


Figure 1. Geometry of Surface #4.

For a detailed description of the wind tunnel facility, refer to Ref. 9. A very brief introduction is given here. Figure 2 is the schematic of the wind tunnel used in Bons' experiment. Fig. 3 shows the dimensions of the test section with the location of six roughness panels. The leading edge of the boundary layer starts from the boundary layer suction point. The cross-section area of the roughness panel sections is 240mm by 380mm. The leading edge of the roughness panel sections are located 1040mm from the boundary layer suction point. Typically, six individual roughness panels (140mm length x 120mm width) are installed in a 280mm stream-wise gap in the lower wall. The tunnel then continues 620mm beyond the trailing edge of the roughness panels.

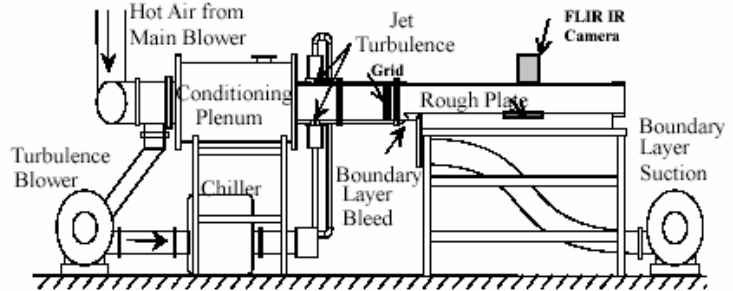


Figure 2. Schematic of the Flat Plate Wind Tunnel in Heat Transfer Measurement Configuration. (Bons GT-2002-30198)

It is a hard job to make precise drag measurements over rough surfaces. Acharya et al.<sup>18</sup> suggested a force-balance method rather than boundary layer momentum balance and log-region curve fitting methods which are velocity based  $c_f$  measurement methods. In Bons' experimental study, a hanging element balance was used to obtain  $c_f$ .

To measure  $St$ , a FLIR Thermacam SC 3000 infrared camera system was mounted with lens fit into a hole in the ceiling of the tunnel. The camera field of view is roughly 70x90mm. The limited field of view is centered at a distance of 1200mm from the leading edge of the tunnel floor. The surface temperatures gotten from the camera were area-averaged to obtain the representative surface temperature history to calculate  $St$ . The Stanton number was determined from this surface temperature history using the method of Schultz and Jones<sup>19</sup>. It is based on Duhamel's superposition method.

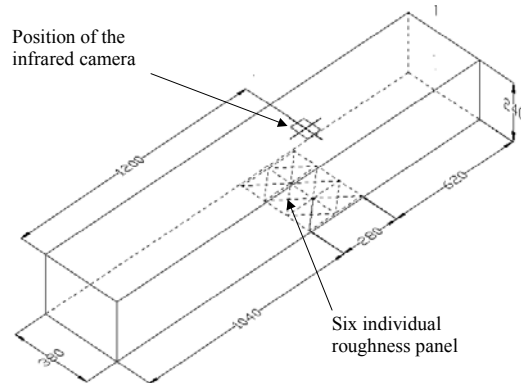


Figure 3. Schematic of the wind tunnel and the position of the roughness panels.

### III. Viscous Cartesian Grid Generation Approach

The first step in a CFD simulation is to define or import the geometry, and generate a computational grid. In a viscous Cartesian grid method, a volume grid is first generated before a surface grid is produced through projections. A unique advantage of the method is that “dirty” geometries may be automatically handled without geometry repair<sup>11</sup>. The generation of a viscous Cartesian grid can be accomplished in the following steps:

#### A. Adaptive Cartesian Grid Generation

Two meshing parameters,  $d_{min}$  and  $d_{max}$  are specified first. They represent the minimum and maximum sizes of Cartesian grid cells to be generated. One of the popular data structures for adaptive Cartesian grids is the Octree. A more flexible data structure is the so called  $2^N$  tree, which supports anisotropic subdivisions. The adaptive Cartesian grid is generated by recursively subdividing a single coarse root Cartesian cell. Since the root grid cell must cover the entire computational domain, the surface geometry is contained in the root cell. The size of the Cartesian cells intersecting the geometry is controlled by two parameters,  $disT$  and  $disN$ . Parameter  $disN$  controls the Cartesian cell size in the geometry normal direction, whereas  $disT$  specifies the Cartesian cell size in the geometry tangential direction. The ratio  $disT/disN$  determines the maximum cell aspect ratio in the Cartesian grid. The recursive subdivision process stops when all the Cartesian cells intersecting the geometries satisfy the length scale requirement. For the sake of solution accuracy, it is very important to ensure that the Cartesian grid is smooth. In the present study, the sizes of any two neighboring cells in any coordinate direction cannot differ by a factor exceeding 2.

#### B. Cartesian Grid Front Generation and Smoothing

In order to “insert” a viscous layer grid between the Cartesian grid and the body surface, Cartesian cells intersected by the geometry must be removed, leaving an empty space between the Cartesian grid and the body surface. All the Cartesian cells intersected by the geometry can be determined efficiently using a tree-based search algorithm. In addition, the intersected cells also serve to divide cells “outside” the geometry from the cells “inside” the geometry. Depending on whether the problem is external or internal, cells “inside” or “outside” the geometry must be removed. The  $2^N$  tree is not only used to record the recursive cell subdivision process, it is also used to perform efficient intersection operations with the geometry. For example, if a (coarse) Cartesian cell does not intersect a geometric entity, all of the child cells from the Cartesian cell must not intersect the geometric entity.

Once the Cartesian cells intersected by the geometry, and cells outside the computational domain are removed, we are left with a “volume” Cartesian grid. The boundary faces of this volume Cartesian grid form the so-called Cartesian front. Before this front is “projected” to the geometry, it is smoothed with a Laplacian smoother to produce a smoother front. To prevent the smoothed Cartesian front from intersecting the body geometry, Cartesian cells which are within a certain distance of the body are also removed.

#### C. Projection of the Cartesian Front to the Body Surface

After the smoothed front in the Cartesian grid is obtained, each node in the front needs to be connected to the body surface to form a single layer of viscous grids. After the front is projected to the boundary geometric entities, a “water-tight” surface grid is generated on the boundary. The “foot prints” of the layer grids on the body surface have the same topology (or connectivity) as the Cartesian front. With this assumption, the viscous layer grids are naturally “blended” with the adaptive Cartesian grid, eliminating the need of cell-cutting currently adopted by many Cartesian grid generators. By connecting each point on the Cartesian front and the corresponding projected point on the boundary, we obtain a single layer of prism grids. This single layer can be sub-divided into multiple layers with proper grid clustering near the geometry to resolve a viscous boundary layer.

An example viscous adaptive Cartesian grid for 2 panels of Surface # 4 (shown in Figure 4) is displayed here. Fig. 5 shows two cutting planes across the computational grid. Note that the viscous layer grid is used to resolve the

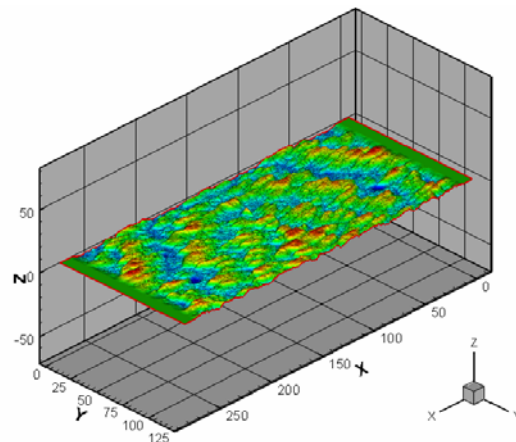


**Figure 4. Geometry of Roughness Surface #4 used in the CFD study. Roughness panel mirrored in the stream-wise direction.**

turbulent boundary layer. The surface grid generated from front projection is displayed in Figure 6. It is observed that the grid cells near the roughness panels are adaptively refined to resolve the roughness elements.

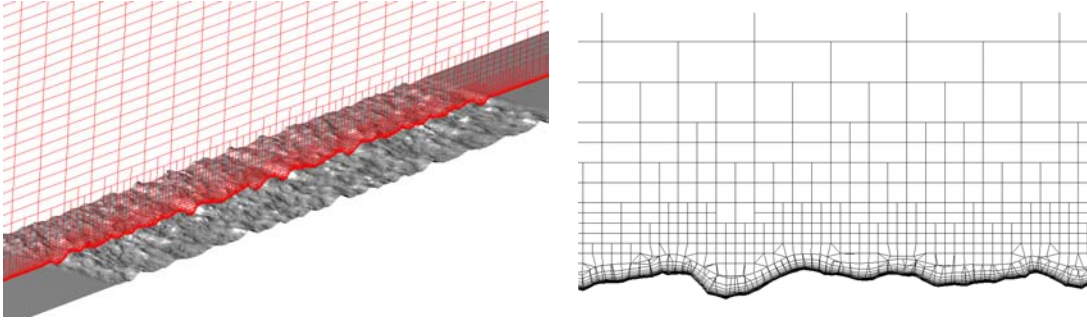


**Figure 5. Cutting planes showing the viscous adaptive Cartesian grids**

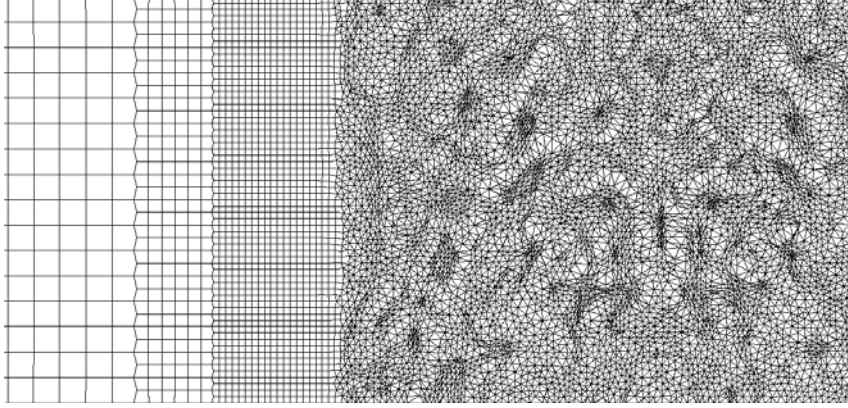


**Figure 6. The surface grid on the lower channel wall showing the refinement near the rough panels.**

#### IV. Numerical Method

A flow solver capable of handling arbitrary polyhedrons has been developed to uniformly handle the adaptive Cartesian and the viscous layer grids<sup>11</sup>. The so-called hanging node problem actually disappears because of the use of a cell-centered finite-volume method supporting arbitrary grid cells. A Cartesian face with a hanging node is actually treated as four separate faces. The hanging nodes are, in fact, not visible to the flow solver. This simple treatment is not only accurate, but fully conservative as well.

The Reynolds-averaged Navier-Stokes equations can be written in the following integral form:

$$\int_V \frac{\partial Q}{\partial t} dV + \oint_S (F - F_v) dS = 0 \quad (1)$$

where  $Q$  is the vector of conserved variables,  $F$  and  $F_v$  are inviscid and viscous flux vectors, respectively. The integration of Eq. (1) in an arbitrary control volume,  $V_i$ , gives:

$$\frac{d\bar{Q}_i}{dt} V_i + \sum_f F_f S_f = \sum_f F_{v,f} S_f \quad (2)$$

where  $\bar{Q}_i$  is the vector of cell-averaged conserved variables,  $F_f$  and  $F_{v,f}$  are the numerical inviscid and viscous flux vectors through face  $f$ , and  $S_f$  is the face area. The overbar will be dropped from here on. The key is then how to compute the inviscid and viscous fluxes through any given face. Here the standard Godunov-type finite volume approach is employed. Using a linear least-squares reconstruction algorithm, a cell-wise linear distribution can be built for each solution variable (in the present study the primitive variables). To compute the inviscid flux, an approximate Riemann solver such as Roe flux difference splitting<sup>20</sup> is used given the reconstructed solutions at both sides of a face. To handle steep gradients or discontinuities, a limiter due to Venkatakrishna<sup>23</sup> is used. The viscous flux is computed using a simple and robust approach presented in Reference 21 without a separate viscous reconstruction.

Although explicit schemes are easy to implement, and are often useful for steady-state, inviscid flow problems, implicit schemes are found to be much more effective for viscous flow problems with highly clustered computational grids. An efficient block LU-SGS (Lower-Upper Symmetric Gauss-Seidel) implicit scheme<sup>24</sup> has been developed for time integration on arbitrary grids. This block LU-SGS (BLU-SGS) scheme takes much less memory than a fully (linearized) implicit scheme, while having essentially the same or better convergence rate than a fully implicit scheme. The BLU-SGS scheme can be used to integrate Eq. (2) with both first or second order accuracy. For steady flow computations, the backward Euler approach is employed, i.e.,

$$\frac{Q_i^{n+1} - Q_i^n}{\Delta t} V_i + \sum_f F_f^{n+1} S_f = \sum_f F_{v,f}^{n+1} S_f. \quad (3)$$

For time accurate computations, we employ a very robust second-order backward difference scheme

$$\frac{4Q_i^{n+1} - 3Q_i^n + Q_i^{n-1}}{2\Delta t} V_i + \sum_f F_f^{n+1} S_f = \sum_f F_{v,f}^{n+1} S_f. \quad (4)$$

To further speed convergence, local time steps are used in Eq. (3). Both Eq. (3) and Eq. (4) are then solved with the BLU-SGS approach. Multiple sub-iterations are utilized to solve Eq. (4) to improve time accuracy.

To simulate flow turbulence, a RANS Spalart-Allmaras (S-A) model and a DES approach are employed. They are briefly described next. The S-A one-equation model<sup>12,13</sup> solves a single partial differential equation for a variable  $\tilde{\nu}$  which is related to the turbulent viscosity. The differential equation is derived by using empiricism and arguments of dimensional analysis, Galilean invariance and selected dependence on the molecular viscosity. The model includes a wall destruction term that reduces the turbulent viscosity in the log layer and laminar sublayer. The equation can be written in the following form

$$\frac{D\tilde{\nu}}{Dt} = c_{b1}\tilde{S}\tilde{\nu} - c_{w1}f_w\left[\frac{\tilde{\nu}}{d}\right]^2 + \frac{1}{\sigma}\left[\nabla \cdot ((\nu + \tilde{\nu})\nabla \tilde{\nu}) + c_{b2}(\nabla \tilde{\nu})^2\right] \quad (5)$$

The turbulent viscosity is determined via,

$$\nu_t = \tilde{\nu}f_{v1}, \quad f_{v1} = \frac{\chi^3}{\chi^3 + c_{v1}^3}, \quad \chi \equiv \frac{\tilde{\nu}}{\nu}, \quad (6)$$

where  $\nu$  is the molecular viscosity. Using  $S$  to denote the magnitude of the vorticity, the modified vorticity is defined as

$$\tilde{S} \equiv S + \frac{\tilde{\nu}}{\kappa^2 d^2} f_{v2}, \quad f_{v2} = 1 - \frac{\chi}{1 + \chi f_{v1}}, \quad (7)$$

where  $d$  is the distance to the closest wall. The wall destruction function is defined as

$$f_w = g \left[ \frac{1 + c_{w3}^6}{g^6 + c_{w3}^6} \right]^{1/6}, \quad g = r + c_{w2}(r^6 - r), \quad r \equiv \frac{\tilde{\nu}}{\tilde{S}\kappa^2 d^2}. \quad (8)$$

The closure coefficients are given by:

$$c_{b1} = 0.1355, \sigma = 2/3, c_{b2} = 0.622, \kappa = 0.41, c_{w1} = \frac{c_{b1}}{\kappa^2} + \frac{1 + c_{b2}}{\sigma}, c_{w2} = 0.3, c_{w3} = 2, c_{v1} = 7.1$$

For the DES approach, a new length scale is defined for DES, i.e.,

$$\tilde{d} = \min(d, C_{DES}\Delta), \quad (9)$$

where  $C_{DES}$  is a constant, and  $\Delta$  is the measure of local mesh spacing, taken to be the maximum distance from the current cell centroid to the centroids of its neighbors. Then the distance to the closest wall  $d$  in the  $S$ - $A$  model is replaced with the new length scale  $\tilde{d}$  to obtain DES. The purpose of using this new length is that in boundary layers,  $\Delta$  far exceeds  $d$  and the standard  $S$ - $A$  model rules since  $\tilde{d} = d$ . The model comes with its experience base and fair accuracy. Away from walls, we have  $\tilde{d} = C_{DES}\Delta$  and the model turns into a simple one equation Sub-Grid-Scale (SGS) model, close to Smagorinsky's in the sense that both make the "mixing length" proportional to  $\Delta$ . On the other hand, the approach retains the full sensitivity to the RANS model's predictions of boundary separation. The model constant  $C_{DES}$  was calibrated at 0.65 through the study of isotropic turbulence<sup>24</sup>.

## V. Results and Discussions

The main objective of this study is to assess how well CFD can predict  $c_f$ ,  $St$  for real rough surfaces by comparing computational results with experimental results and correlation formulas. First, turbulent flow over a smooth flat plate in a wind tunnel is computed to validate the finite volume flow solver. Following the validation, computations with rough surfaces in the wind tunnel are performed, and comparisons are made to assess the adequacy of the CFD results.

### A. Turbulent Flow over a Flat Plate in a Wind Tunnel

This case serves two purposes. One purpose is to validate the  $S$ - $A$  model and DES approach in the flow solver. The other is to see how well CFD results agree with correlation formulas and experimental data for smooth walls.

The computational domain is the wind tunnel shown in Fig. 2. To further reduce the computational cost, only 1/6 of the span is included in the computational domain. Symmetry or slip wall boundary conditions are used on the two end walls in the span-wise direction. Therefore the flow is essentially two-dimensional. Two viscous adaptive Cartesian meshes were generated for this case. The coarse mesh has 37,888 cells while the fine mesh has 58,368 cells. The average  $y^+$  value of the first cell from the wall is 0.8 for the coarse mesh and 0.3 for the fine mesh. Simulations were carried out using the  $S$ - $A$  models on both meshes. Figure 7 shows the computed average  $c_f$  and  $St$  over the area where roughness panels are located and the experimental and correlation values. Standard flat plate correlations for  $c_f$  and  $St$ <sup>28</sup> are calculated as follows:

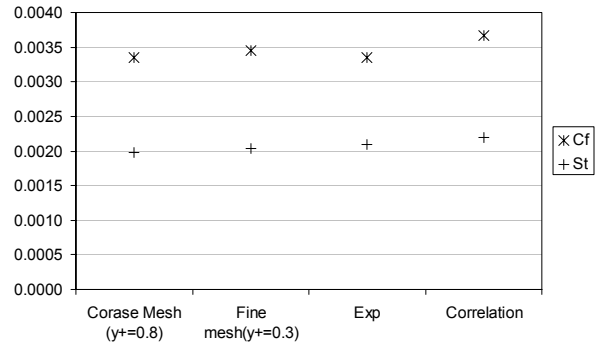


Figure 7. CFD simulation results compared to experimental data and standard roughness correlations.

$$c_f = \frac{0.026}{\text{Re}_x^{1/7}}$$

$$St = \frac{0.5c_f}{\text{Pr}_t + \sqrt{0.5c_f [5\text{Pr} + 5\ln(5\text{Pr} + 1) - 14\text{Pr}_t]}}$$

Note that the computed  $c_f$  and  $St$  on the coarse grid agree quite well with those on the fine grid indicating the grid resolution is adequate for the present simulation. The computed  $c_f$  and  $St$  are also in good agreement with the experiment and correlation results. The computational results suggest that the S-A model is capable of predicting both  $c_f$  and  $St$  for the flat plate case.

Next, both S-A and DES approaches are studied and compared on the fine mesh. For the S-A model, a local time stepping strategy with a CFL of 50 was employed. For the DES approach, the simulation must be carried out in a time-accurate manner. Therefore to study temporal convergence, two cases were performed with different time steps. In the case of DES1, the time step is  $2.457e-4$  (which corresponds to a CFL number of 1000 for the smallest cell), while the time step is doubled for the case of DES2. The convergence histories of  $c_f$  and  $St$  from all three simulations are plotted in Fig. 8 in terms of the number of iterations or time steps. In terms of physical time, both DES cases showed identical convergence histories, indicating the simulation is time-step independent. Note that

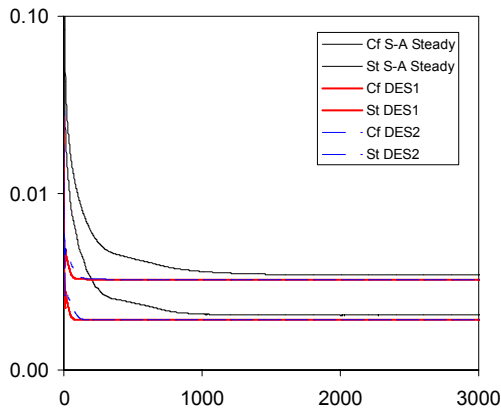


**Figure 8. Convergence histories for flat panels with S-A and DES approaches**

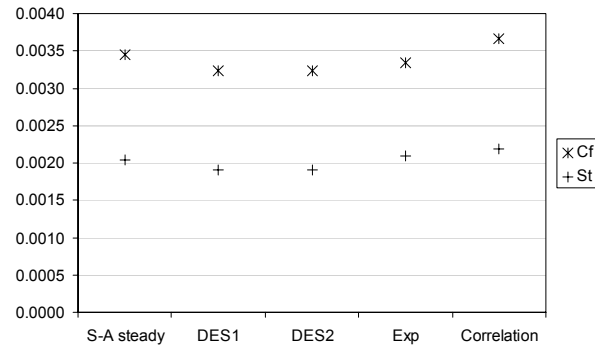


**Figure 9. Comparison of CFD results for flat panels using S-A and DES approaches with experimental and correlation data.**

convergence in  $c_f$  and  $St$  was achieved in about 2000 iterations for the S-A model, and in about 200 time steps for the DES approach. The convergence for the DES approach is a lot faster because of the larger time step in the viscous boundary layer and the use of multiple sub-iterations to achieve time accuracy. Figure 9 shows the computed average  $c_f$  and  $St$  with comparison to experimental data and correlation formula. It is observed that the DES approach predicted a slightly lower value of  $c_f$  and  $St$  than the S-A model.

## B. Turbulent Flow over Rough Surfaces in a Wind Tunnel

A set of studies using the flat panel indicated that the computational grid should have a  $y^+$  value of 1 for the cells near a no-slip wall. Since the smaller the  $y^+$  value, the more CPU time is needed to achieve solution convergence. For all the simulations with roughness panels, the average  $y^+$  value of the first grid layer near the wall is near unity.

As mentioned earlier, two rough surfaces (Surface #4 and #6 from Reference 9) were employed in the present study. In addition, two different grids were generated for each surface. For example, for Surface #4, the coarse grid has 364,005 total cells with 108,709 hexahedron, 234,952 prism cells and 20,344 polyhedral cells, while for the fine grid it has a total of 1,260,051 cells with 400,662 hexahedrons, 782,340 prisms, and 77,049 polyhedral cells. For Surface #6, the coarse and fine grids have 873,221 and 1,601,430 cells respectively. The fine grid essentially doubles the grid resolution near the roughness panels while maintaining an average  $y^+$  of 1 in the wall normal direction. The coarse mesh has 64 cells in the span-wise direction with a grid resolution of about 1 mm, while the fine mesh has a grid resolution of about 0.5 mm. The fine grids have about 50-80 layers in the tunnel height direction. If structured grids were used for this configuration, the fine grid then would have about 25-40 million cells. Using the viscous adaptive Cartesian grid approach, the number of grid cells can be reduced by over an order of magnitude. All the grids look similar to those shown in Figures 5 and 6.

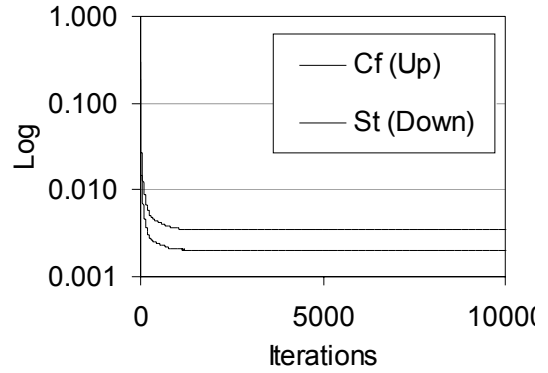


**Figure 10. Convergence histories using the S-A model with the fine mesh for Surface #4.**

All the simulations using the S-A model were carried out with a local time stepping strategy and all the DES runs were in time accurate mode with a 2<sup>nd</sup>-order backward difference formula. The flow convergence is monitored by the history of the average  $c_f$  and  $St$  over the roughness panels. For example, Fig. 10 shows the convergence history of the average  $c_f$  and  $St$  using the S-A model on the fine grid for surface #4. Note that the solution is converged after a few thousands of iterations.

Table 1 summarizes the computational results with comparison to experimentally measured  $c_f$  and  $St$ . The computed average  $c_f$  and  $St$  on the coarse and fine meshes still show large discrepancies, indicating the coarse grid is just too coarse. In order to demonstrate grid convergence, an even finer grid is necessary. On the fine grid, the results are more encouraging. With both rough surfaces, the computed  $c_f$  number is within 3.5% of the experimental data. The difference between the computed and measured  $St$  numbers is larger at about 15% for Surface #4 and 8% for Surface #6 on the fine grids. This difference may be due to several factors. One factor is that a constant wall temperature was used in the computation. In the actual experiment, the wall temperature is not constant. Another factor is insufficient grid resolution. It appears that  $St$  increases with grid refinement. Further investigation with finer grids and non-constant wall temperature will be carried out to find the reason. The computed  $c_f$  and  $St$  using DES are too large, and the cause will be investigated.

**Table 1. Comparison of experimental and computational results for roughness Surfaces # 4 and #6**

	Surface #4 (Coarse)	Surface #4 (Fine)	Surface #4 (Experiment)	Surface #4 (DES after 5000 time steps)	Surface #6 (Coarse)	Surface #6 (Fine)	Surface #6 (Experiment)
$c_f$	0.0128	0.00970	0.00937	0.0317	0.0113	0.0100	0.0103
$St$	0.00255	0.00260	0.00308	0.0111	0.0259	0.00284	0.00308

The computational results are also compared with four roughness correlations and the experimental data in Figures 11 and 12 at  $Re_x = 900,000$ . These correlation formulas are given below.

$$c_f = [1.4 + 3.7 \log(x/k_s)]^{-2} \quad \text{from White}^{26}$$

$$c_f = [2.87 + 1.58 \log(x/k_s)]^{-2.5} \quad \text{from Schlichting}^{27}$$

$$c_f = [3.476 + 0.707 \ln(x/k_s)]^{-2.46} \quad \text{from Mills}^{28}$$

$$c_f = 0.168 [\ln(84\delta/k_s)]^{-2} \quad \text{from Kays and Crawford}^{29}$$

The  $k_s$  value in these correlations were computed based on  $\Lambda_s$  which was tabulated in Table 1 of Ref. 9.

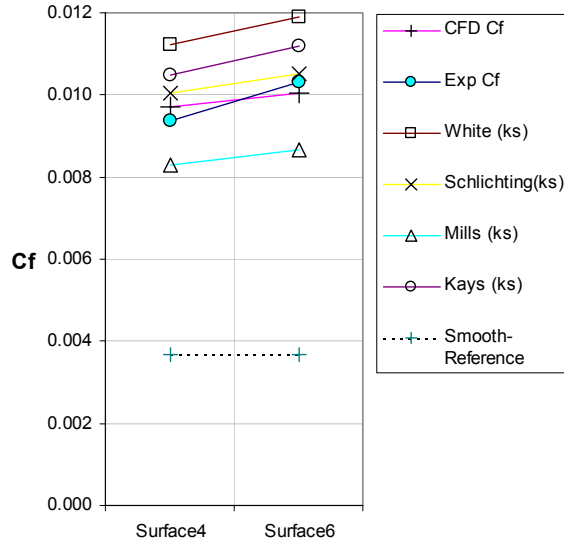


**Figure 11. Comparison of Skin frictions for roughness panels**

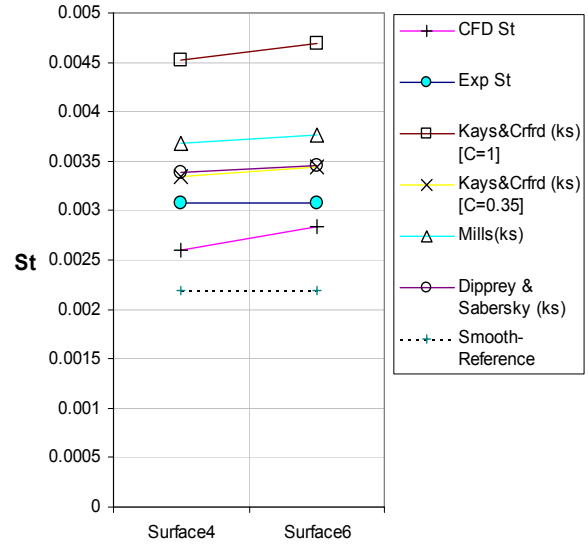


**Figure 12. Comparison of Stanton numbers for roughness panels**

The dashed line in Figure 11 is the  $c_f$  number of the smooth panel as a reference. As shown in Figure 11, the computed  $c_f$  matches the experimental data very well. The Schlichting correlation also gives good prediction. All the correlations appear to bound the experimental and CFD data. This may suggest that CFD can be used as an effective tool to predict  $c_f$  for “real” rough surfaces.

The  $St$  results are compared in Figure 12. In this graph, three correlations are used for comparison

$$S_t = \frac{0.5c_f}{Pr_t + \sqrt{0.5c_f} (k^{+0.2} Pr^{0.44}/C)} \quad \text{from Kays and Crawford}^{29}$$

$$S_t = \frac{0.5c_f}{1 + \sqrt{0.5c_f} (5.19k^{+0.2} Pr^{0.44} - 8.5)} \quad \text{from Dipprey and Sabersky}^{30}$$

$$S_t = \frac{0.5c_f}{Pr_t + \sqrt{0.5c_f} (4.8k^{+0.2} Pr^{0.44} - 7.65)} \quad \text{from Wassel and Mills}^{31}$$

In all the correlation formulas, the  $c_f$  value predicted with the Schlichting correlation is selected as the reference since it has the best agreement with experimental and CFD data. As shown in Figure 12, CFD gives the lowest  $St$  prediction. Comparing with the experimental data, all correlations predict higher rough surface  $St$  numbers.

Since CFD can provide more detailed flow field data, a few “flow pictures” are shown here to give the reader some ideas on the flow characteristics. A velocity vector plot showing the flow near the rough panel is displayed in Fig. 13. It is observed that very complex separated flow regions exist near the rough surfaces. The surface pressure distribution near the rough panel of Surface #6 on the fine grid is shown in Fig. 14. Clearly on the rough surfaces, the pressure drag is a dominant force in the overall drag. In fact, over 75% of the total drag is due to pressure in both cases.

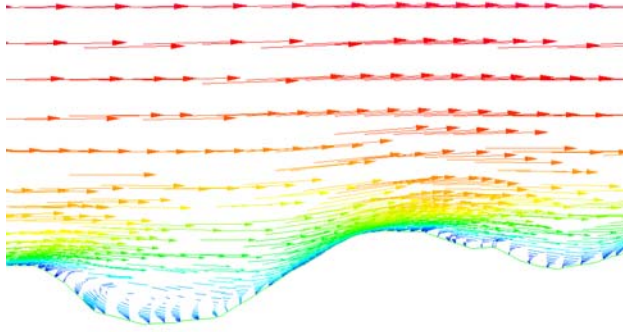


**Figure 13. Velocity vector plot on a cutting plane near the roughness panel**

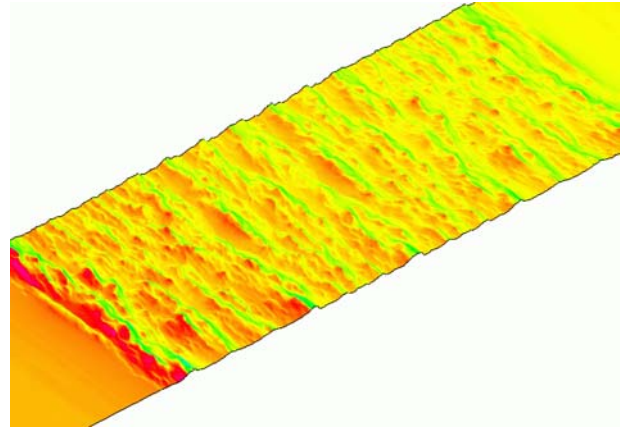


**Figure 14. Pressure distribution on the rough surface (Surface #6).**

## VI. Conclusions

In the present study, the skin friction ( $c_f$ ) and heat transfer ( $St$ ) coefficient on real rough surfaces are directly computed using a state-of-the-art unstructured adaptive grid-based finite volume flow solver. Both RANS and DES approaches are employed for the computations. Computational results are compared with experimental data to assess the simulation accuracy. Based on the present study, the following conclusions can be drawn:

1. The unstructured adaptive grid generation method is very efficient in resolving disparate length scales. It is estimated that the number of cells generated is over an order of magnitude less than that with a structured grid. The rough surfaces can be handled by the grid generator with minimum user interference;
2. On the flat panel case, both the S-A and DES approaches are capable of predicting  $c_f$  and  $St$ , thus validating the implementation;
3. With proper grid resolution, the S-A model was able to accurately predict  $c_f$  for both rough surfaces (within 3.5% of experimental data). The computational predictions for  $St$  showed 8-15% differences from the experimental data. This could be attributed to the constant wall temperature used in the computational simulation, or insufficient grid resolutions. Further investigation will be carried out to understand why.
4. The DES approach has failed to predict either  $c_f$  or  $St$  for both rough surfaces. It is believed that the time accurate computations with DES have not reached a statistically steady-state. We plan to use a newly built parallel cluster to carry out the expensive unsteady computations.

In addition, finer computational grids will be used to further assess grid convergence for the cases with rough surfaces.

## Acknowledgements

The authors gratefully acknowledge the support from the DOE University Turbine Systems Research (UTSR) Program.

## References

- <sup>1</sup>Goldstein, R., Eckert, E., Chiang, H., and Elovic, E., "Effect of Surface Roughness on Film Cooling Performance," ASME Journal of Engineering for Gas Turbines and Power, January 1985, Vol. 107, pp. 111-116.
- <sup>2</sup>Pinson, M.W. and Wang, T., "Effects of Leading Edge Roughness on Fluid Flow and Heat Transfer in the Transitional Boundary Layer over a Flat Plate," International Journal of Heat and Mass Transfer, 1997, Vol. 40, No. 12, pp. 2813-2823.
- <sup>3</sup>Taylor, R.P., Scaggs, W.F., and Coleman, H.W., 1988, "Measurement and Prediction of the Effects of Non-uniform Surface Roughness on Turbulent Flow Friction Coefficients," ASME Journal of Fluids Engineering, Vol. 110, Dec 1988, pp. 380-384.
- <sup>4</sup>Hosni, M.H., Coleman, H.W., and Taylor, R.P., 1991, "Measurements and Calculations of Rough-Wall Heat Transfer in the Turbulent Boundary Layer," International Journal of Heat and Mass Transfer, Vol. 34, No. 4/5, pp. 1067-1082.
- <sup>5</sup>Scaggs, W.F., Taylor, R.P., and Coleman, H.W., "Measurement and Prediction of Rough Wall Effects on Friction Factor - Uniform Roughness Results," ASME Journal of Fluids Engineering, Vol. 110, Dec 1988, pp. 385-391.
- <sup>6</sup>Bogard, D.G., Schmidt, D.L., and Tabbita, M., "Characterization and Laboratory Simulation of Turbine Airfoil Surface Roughness and Associated Heat Transfer," Journal of Turbomachinery, Vol. 120, No. 2, April 1998, pp. 337-342.

- <sup>7</sup>Barlow, D.N. and Kim, Y.W., 1995, "Effect of Surface Roughness on Local Heat Transfer and Film Cooling Effectiveness," presented at the June, 1995 ASME International Gas Turbine Exposition in Houston, Texas, ASME paper #95-GT-14.
- <sup>8</sup>Bons, J.P., Taylor, R., McClain, S., Rivir, R.B., "The Many Faces of Turbine Surface Roughness," *Journal of Turbomachinery*, Vol. 123, No. 4, October 2001, pp. 739-748
- <sup>9</sup>Jeffrey P. Bons, "St and Cf augmentation for real turbine roughness with elevated freestream turbulence," *Proceeding of TURBOEXPO 2002: International gas turbine conference June 3-6, 2002 in Amsterdam, The Netherlands.*
- <sup>10</sup>Wang, Z.J. and Srinivasan, K., 2002, "An Adaptive Cartesian Grid Generation Method for 'Dirty' Geometry," *International Journal for Numerical Methods in Fluids*, vol. 39, pp. 703-717.
- <sup>11</sup>Wang, Z.J. and Chen, R.F., 2002, "Anisotropic Solution-Adaptive Viscous Cartesian Grid Method for Turbulent Flow Simulation," *AIAA Journal*, vol. 40, pp. 1969-1978.
- <sup>12</sup>Spalart, P.R., Allmaras, S.R., "A one-equation turbulence model for aerodynamic flows," AIAA-92-0439
- <sup>13</sup>Spalart, P.R., Allmaras, S.R., 1994. "A one-equation turbulence model for aerodynamic flows," *La Recherche A erospatiale* 1, 5-21
- <sup>14</sup>Spalart, P.R., Jou, W.-H., Strelets, M., Allmaras, S.R., 1997. "Comments on the feasibility of LES for wings, and on a hybrid RANS/LES approach," In: Liu, C., Liu, Z. (Eds.), *First AFOSR International Conference on DNS/LES*, 4-8 August, Ruston, LA, *Advances in DNS/LES*, Greyden Press, Columbus, OH.
- <sup>15</sup>P. R. Spalart, "Strategies for turbulence modeling and simulations," *International Journal of Heat and Fluid Flow* 21(2000) p252-263
- <sup>16</sup>Spalart, "Trends in turbulence treatments," *AIAA Paper 2000-2306*, Fluids 2000, Denver.
- <sup>17</sup>Nikuradse, J., 1933, "Laws for Flows in Rough Pipes," *VDI-Forschungsheft* 361, series B, Vol. 4. (English Translation NACA TM 1292, 1950)
- <sup>18</sup>Acharya, M., Bornsterin, J., Escudier, M., 1986, "Turbulent Boundary Layers on Rough Surfaces," *Experiments in Fluids*, No 4, pp. 33-47
- <sup>19</sup>Schultz, D.L. and Jones, T.V., 1973, "Heat-transfer Measurements in Short-duration Hypersonic Facilities," *Advisory Group for Aerospace Research and Developments*, No. 165, NATO
- <sup>20</sup>Roe, P. L., "Approximate Reimann Solvers, Parameter Vectors, and Difference Schemes," *Journal of Computational Physics*, Vol. 43, 1983, p.357.
- <sup>21</sup>Wang, Z.J., "A Quadtree-Based Adaptive Cartesian/Quad Grid Flow Solver for Navier-Stokers Equations," *Computers and Fluids*, vol. 27, No. 4, 1998, pp. 529-549.
- <sup>22</sup>Wang, Z.J., "Proof of Concept - An Automatic CFD Computing Environment with a Cartesian/Prism Grid Generator, Grid Adaptor and Flow Solver," *Proceedings of 4<sup>th</sup> International Meshing Roundtable*, Sandia National Labs, Albuquerque, NM, 1995, pp.87-99.
- <sup>23</sup>Venkatakrishnan, V., "Convergence to Steady State Solutions of the Euler Equations on Unstructured Grids with Limiters," *Journal of Computational Physics*, Vol. 118, 1995, pp. 120-130.
- <sup>24</sup>Chen, R.F., and Wang, Z.J., "Fast, Block Lower-Upper Symmetric Gauss-Seidel Scheme for Arbitrary Grids," *AIAA Journal*, Vol. 38, No. 12, 2000, pp. 2238-2245
- <sup>25</sup>Shur, M., Spalart, P.R., Strelets, M., Travin, A., 1999. "Detached-eddy simulation of an airfoil at high angle of attack," *Proceedings of the Fourth International Symposium on Engineering Turbulence Modeling and Measurements*, 24-26 May, Corsica, Elsevier, Amsterdam.
- <sup>26</sup>White, F.M., *Viscous Fluid Flow*, 2nd Edition, 1991, McGraw-Hill, New York.
- <sup>27</sup>Schlichting, H. *Boundary layer Theory*, 7th Editon, 1979, McGraw-Hill, New York
- <sup>28</sup>Mills, A.F., *Heat transfer*, 2st Edition, Prentice-Hall, New Jersey. ISBN 0-13-947624-5 .
- <sup>29</sup>Kays, W.M., Crawford, M.E., *Convective Heat and Mass Transfer*, 3rd Edition, 1993, McGraw-Hill, New York
- <sup>30</sup>Dippery, D.F, and Sabersky, R.H, "Heat and Momentum Transfer in Smooth and Rough Tubes at Various Prandal Numbers," *International Journal of Heat and Mass Transfer*, Vol. 6, pp.329-353
- <sup>31</sup>Wassel, A.T. and Mills, A.F., "Calculating of Variable Property Turbulent friction and Heat Transfer in Rough Pipes," *Journal of Heat Transfer*, Vol. 101 August 1979, pp.469-474